

Dynamic polarization control of Ni electrodes for sustainable and scalable water electrolysis under alkaline conditions

Received: 21 June 2024

Accepted: 14 May 2025

Published online: 23 May 2025

Sanghwi Han¹, Sungjun Kim², Hye Jin Cho², Jang Yong Lee³✉, Jaeyune Ryu^{1,4,5}✉ & Jeyong Yoon^{1,5}✉

Despite the wide array of oxygen evolution reaction active materials revealed thus far, challenges persist in translating their half-cell scale activities into scalable devices with long-term durability. Here, we present a dynamic polarization control for the continuous electrochemical activation of readily available Ni electrode anodes to achieve sustainable and scalable water electrolysis. Periodic application of a reductive potential between high current density cycles (0.5 or 1 A cm⁻²) is found to promote and maintain the oxygen evolution activity of Ni electrodes via the incorporation of Fe³⁺ from KOH electrolytes. This transient polarization strategy successfully extends to an anion exchange membrane water electrolysis system, where a cell voltage of approximately 1.8 V is maintained for over 1000 h under 1 A cm⁻². The scalability is further verified by the 25 cm² 3-cell stack system, which lasts for 300 h with negligible voltage loss. Ultimately, this work highlights the power of the dynamic polarization strategy to regulate the dynamic nature of the oxygen evolution interface for sustainable and scalable water electrolysis.

Recent advancements in electrocatalysts have been reshaping energy conversion technologies, offering promising alternatives to conventional fossil fuel-based energy systems. Central to this transformation is the oxygen evolution reaction (OER), a pivotal electrochemical process that can be combined with versatile cathodic reactions for a wide range of energy applications such as water electrolysis^{1–7}, metal/air batteries^{8,9}, and CO₂ electrolysis^{10–12}. Despite the plethora of OER active materials discovered to date, including noble-metal oxides (e.g., RuO₂ and IrO₂)^{13,14}, perovskite-type oxide structures¹⁵, and 3d transition-metal-based hydr(oxy)oxides^{16–20}, challenges persist in translating their half-cell scale activities into an upscaled functional device with long-term durability^{21,22}.

The OER interface is inherently dynamic. Under applied bias, active materials undergo continuous structural evolutions, such as phase transitions, dissolution, and deposition, governed by the

interplay between electrode surfaces and electrolyte species^{23–32}. High OER turnover typically coincides with increased metal dissolution, underscoring the delicate stability of active sites during operation. Recent reports on Fe-incorporated (hydr)oxides highlight the critical need to balance Fe dissolution and redeposition kinetics to sustain dynamically stable and catalytically competent surfaces (Fig. 1, middle)^{1,33,34}. To this end, strategies have been developed to chemically modulate host materials, tuning Fe binding energies to promote this balance and improve both activity and durability^{1,35–37}. However, these approaches have so far fallen short of shifting the stability window to accommodate practically relevant current densities (e.g., >50 mA cm⁻²). At higher overpotentials—required for real-world applications—dissolution rates often outpace redeposition, resulting in the progressive loss of active sites and degradation of OER performance over time (Fig. 1, right)^{21,35,37}.

¹School of Chemical and Biological Engineering, Institute of Chemical Processes, Seoul National University (SNU), Seoul, Republic of Korea. ²Hydrogen Energy Research Center, Korea Research Institute of Chemical Technology (KRICT), Daejeon, Republic of Korea. ³Department of Chemical Engineering, Konkuk University, Seoul, Republic of Korea. ⁴Center for Nanoparticle Research, Institute for Basic Science (IBS), Seoul, Republic of Korea. ⁵SNU Energy Initiative, Seoul National University (SNU), Seoul, Republic of Korea. ✉e-mail: ljyly78@konkuk.ac.kr; jaeyune.ryu@snu.ac.kr; jeyong@snu.ac.kr

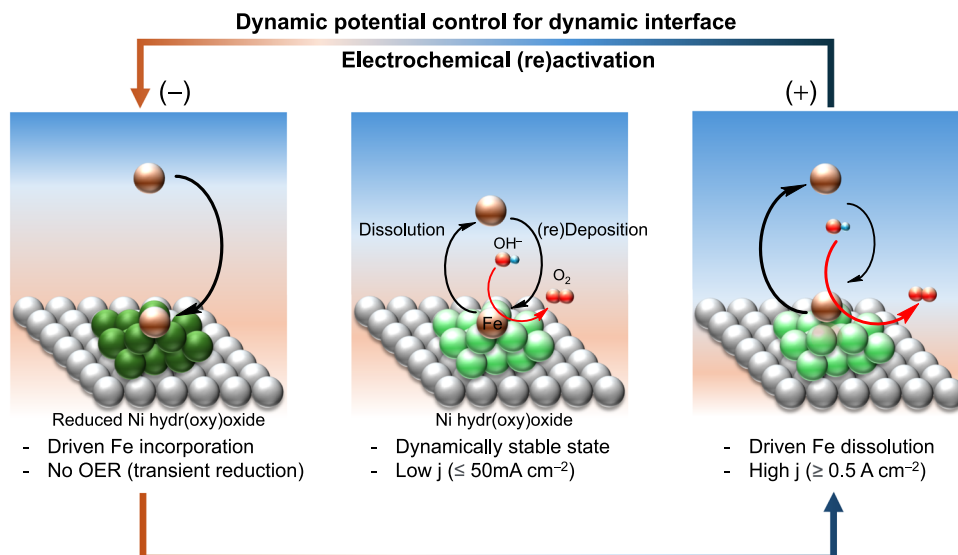


Fig. 1 | Dynamic polarization control for continuous activation and reactivation of Fe-incorporating Ni hydr(oxy)oxide. The OER interface tends to deviate from the suggested dynamically stable state (middle), resulting in a loss of activity due to the dissolution of active sites driven by high current operation (0.5 or 1 A cm^{-2}) (right). Applying a transient reductive bias on Ni-based electrodes between OER cycles at high current densities promotes the (re)deposition of Fe from electrolytes (left), serving as a compensatory process for regenerating active

sites. This dynamic polarization control leads to additional activation of the Ni electrodes by augmenting the incorporation of Fe from the electrolytes. The black arrow pointing upward symbolizes Fe dissolution, while the downward arrow denotes Fe (re)deposition, with the size of the arrows indicating the relative amount involved. The color codes: Fe in brown, Ni hydro(oxy)oxide in green, reduced Ni hydro(oxy)oxide in dark green, metallic Ni in gray, oxygen (O) in red, and hydrogen (H) in blue.

To overcome this limitation, we present an electrochemical activation (EA) strategy designed to compensate for the dissolution-induced degradation of active sites at high current densities. Using readily available Ni-based electrodes (Ni felt, foam, mesh, and foil), we demonstrate that the periodic application of a reductive potential between OER cycles at $0.5\text{--}1 \text{ A cm}^{-2}$ triggers the redeposition of Fe^{3+} from the electrolyte onto the Ni surface (Fig. 1, left). This dynamic polarization control not only mitigates site loss but also promotes further activation of the Ni electrode by continuously regenerating catalytically active Fe-Ni hydr(oxy)oxide species. Unlike strategies requiring elaborate electrode design, this transient protocol is readily implementable across simple electrode formats, enhancing its scalability. Crucially, the benefits of this EA approach extend beyond the half-cell level. In an anion exchange membrane water electrolyzer (AEMWE), we achieve stable operation at 1 A cm^{-2} with a cell voltage of $\sim 1.8 \text{ V}$ maintained over 1000 h. Moreover, a 25 cm^2 three-cell stack equipped with this protocol operates continuously for over 300 h with negligible voltage loss. Together, these results establish dynamic polarization as a powerful strategy for regulating the redox environment at the OER interface, offering a scalable and durable route for next-generation water electrolysis.

Results

Electrochemical activation and reactivation

We first evaluated the effect of EA operation on the OER performance of readily available Ni felt (NF) electrodes. The EA protocol adopts repeating OER cycles in 1 M KOH electrolytes at a constant current density of 0.5 A cm^{-2} for 1 h, followed by a 3 min activating at constant potential (Fig. 2a). Applying the potential at 0.6 V vs. reversible hydrogen electrode (RHE), $0.6 V_{\text{RHE}}$, during EA, gave rise to continuous activation and reactivation of the NF for its 50-time runs spanning 50 h (Fig. 2b). Before and after applying the reductive potential during EA, however, the NF showed immediate increases in overpotentials (black arrow in Fig. 2b) which indicate that our high current density condition (0.5 A cm^{-2}) favors the dissolution of active sites (Fig. 1, right). Degrees of the activation and reactivation gradually decrease as OER overpotential decreases upon repeating EA,

suggesting continuous and gradual transitions of catalyst structure into its dynamically stable steady-state. Compared to the normal operation of OER without EA (w/o EA), the EA protocol for the same duration (50 cycles over 50 h) resulted in a decrease in overpotential at 0.5 A cm^{-2} ($\eta_{50\text{h}} - \eta_{0\text{h}}$), with the most pronounced effect observed when the NF was poised at $0.6 V_{\text{RHE}}$ during EA operation (Fig. 2c and Supplementary Figs. 1–3). The bare NF experienced activity enhancements when the transient potential was applied below $1.2 V_{\text{RHE}}$ during EA operation, suggesting a critical role of reductive environments in activating NF (Supplementary Fig. 3). In addition, we tested at 0 and $-0.3 V_{\text{RHE}}$, as well as at 0.9 and $0.6 V_{\text{RHE}}$. The experimental results demonstrated consistent outcomes across these conditions, with a reduction in overpotential of $\sim 280 \text{ mV}$ observed during 50 h of EA operation, indicating that a more reductive potential is unnecessary below $0.9 V_{\text{RHE}}$ (Supplementary Fig. 4). Minimal differences in electrochemical active surface areas (ECSAs) determined by non-Faradaic double layer capacitance measured after 50 h of EA operations with varying reductive potentials (Supplementary Fig. 5) suggest that the observed trend in catalyst activation is attributed to a differential induction of an active phase or active sites, which is not simply commensurate with the ECSAs.

Electrochemical characterization of NF reveals that our EA protocol facilitates the evolution of the surface structure into an OER-active NiOOH -type phase. Before experiencing 50 h operation, NF initially exhibited a redox feature of $\alpha\text{-Ni}(\text{OH})_2/\gamma\text{-NiOOH}$ (at $1.33 V_{\text{RHE}}$ for oxidation and $1.25 V_{\text{RHE}}$ for reduction) (Fig. 2d, black), consistent with previous reports^{34,38,39}. While 50 h operation w/o EA led to an additional redox feature of $\beta\text{-Ni}(\text{OH})_2/\beta\text{-NiOOH}$ (at $1.37 V_{\text{RHE}}$ for oxidation and $1.2 V_{\text{RHE}}$ for reduction) (Fig. 2d, blue), 50 h of EA operation regenerates a redox feature of $\alpha\text{-Ni}(\text{OH})_2/\gamma\text{-NiOOH}$ with an increased magnitude (Fig. 2d, red). When EA operation was conducted with potentials below $1.2 V_{\text{RHE}}$, the peak of the oxidative current density of the $\alpha\text{-Ni}(\text{OH})_2/\gamma\text{-NiOOH}$ increased by more than fourfold compared to the initial level (Supplementary Fig. 6 and Supplementary Fig. 7). All CV data were iR-corrected using the ohmic resistance ($0.9 \pm 0.1 \Omega \text{ cm}^2$) obtained from EIS analysis and a geometric area of 1 cm^2 . The non-iR-corrected CV data are presented in Supplementary Fig. 6e.

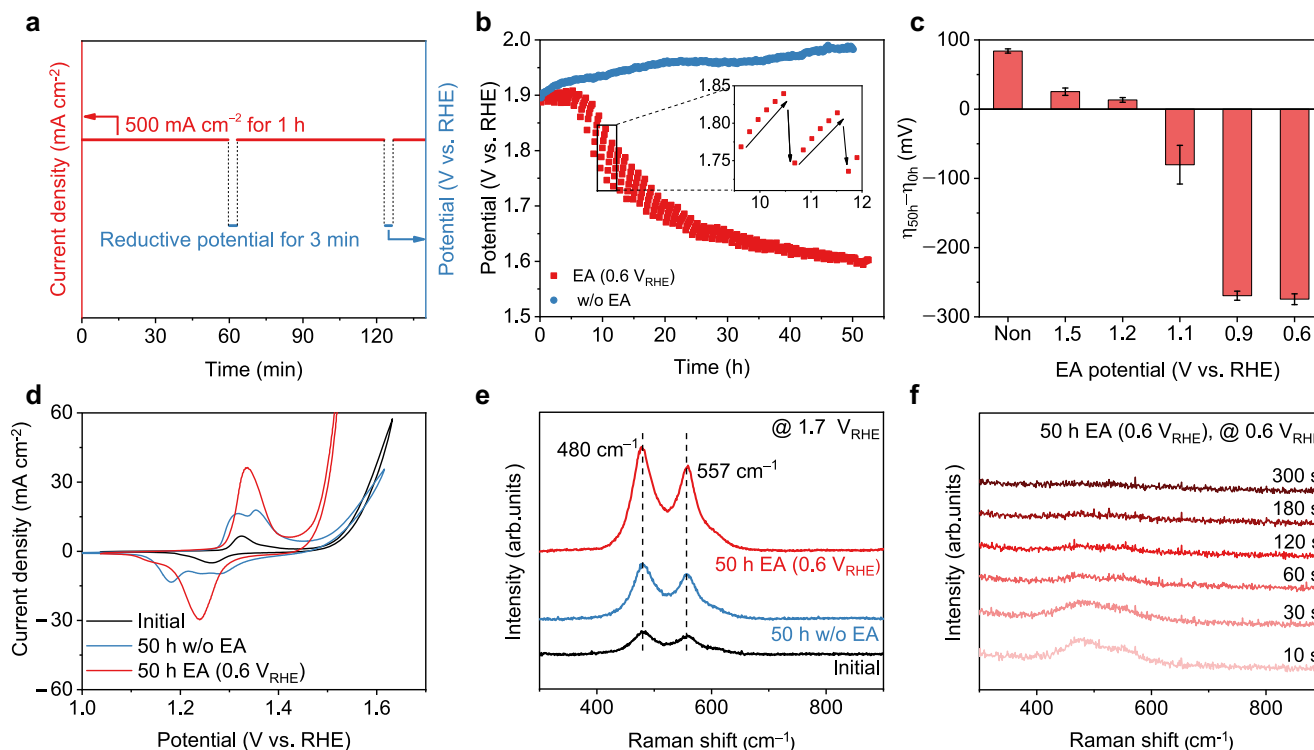


Fig. 2 | EA operation in half-cell systems. **a** EA conditions for half-cell systems. **b** iR-corrected potential traces of NF at 0.5 A cm^{-2} with and w/o EA operation in a 1 M KOH solution. Data were collected at 10 min intervals during 1 h application of 0.5 A cm^{-2} , and at 1 min intervals during 3 min application of a reductive activating potential. The black arrow in **(b)** indicates the sequence of this data collection. **c** Overpotential difference before (η_{10h}) and after (η_{50h}) 50 h of EA operation with

varying reductive activating potentials. **d** iR-corrected CV scans of NF at the initial state, after 50 h of normal OER operation, and after 50 h of EA operation with a scan rate of 20 mV s^{-1} . **e** In situ Raman spectra of NF at $1.7 \text{ V}_{\text{RHE}}$ at the initial state, after 50 h of normal OER operation, and after 50 h of EA operation. **f** In situ Raman spectra of NF over time at $0.6 \text{ V}_{\text{RHE}}$ after 50 h of EA operation. Error bars indicate standard errors obtained from 3 or more independent replicates.

In situ Raman spectroscopy further evinces the enhanced induction of the NiOOH phase upon the EA operation. When the NF electrode is poised at the OER operating potential, $1.7 \text{ V}_{\text{RHE}}$, it shows the characteristic NiOOH phase Raman features of which magnitude increases with applying EA (Fig. 2e and Supplementary Fig. 8)^{40,41}. The increased intensity also corresponds to the duration for which the phase persists when the electrode is reduced at $0.6 \text{ V}_{\text{RHE}}$. While the anodically induced NiOOH phases at $1.7 \text{ V}_{\text{RHE}}$ before and after experiencing 50 h of normal operation vanished within 10 s and 30 s, respectively, at $0.6 \text{ V}_{\text{RHE}}$ (Supplementary Fig. 9), the activated NiOOH phase generated after 50 h EA operation persisted for 3 min (Fig. 2f). This time-trace result, in conjunction with the observed maximized OER activation with activation for 3 min compared to other time durations in the EA protocol (Fig. 5d), concludes that complete reduction of NiOOH phase upon repeating EA cycles is critical for full activation of NF.

The role of Fe incorporation in electrochemical activation

Previous research indicates that the γ -NiOOH phase can be produced through electrochemical conditioning methods like CV; however, the abundance of γ -NiOOH alone does not necessarily enhance OER performance^{34,38,39,42}. Rather, it is the incorporation of Fe into γ -NiOOH that has been shown to significantly improve OER activity, outperforming β -NiOOH. Given that the unpurified 1 M KOH electrolyte used for the above studies naturally contains 76 ppb of Fe, as measured by inductively coupled plasma-mass spectrometry (ICP-MS), we posit that the application of a transiently reducing environment may facilitate the incorporation of Fe from the electrolytes to NF (Fig. 1, left). This presumed scenario is consistent with the observed activation of NF with selective emergence of γ -NiOOH phase upon the EA

operation with transient reductive potentials below $1.2 \text{ V}_{\text{RHE}}$ where NiOOH is reduced to Ni(OH)_2 (Fig. 2d).

To examine the Fe incorporation effect, we compared EA behaviors of the same NF electrode in three different 1 M KOH solutions: unpurified KOH, 99.99% KOH, and purified KOH (see details in the Methods section), containing -76, 50, and 20 ppb of Fe, respectively. Our control experiments revealed increasing OER activation with higher Fe content, which is consistent with our expectations. Following 50 cycles of CVs in unpurified KOH, the NF electrode exhibited a reduction of overpotentials at 10 mA cm^{-2} by approximately 50 mV (Fig. 3a, red), greater than the observed 25 mV reduction in 99.99% KOH solution (Fig. 3a, blue). In the purified KOH, however, the activation effect effectively vanishes (Fig. 3a, purple). In all tested electrolytes, the $\text{Ni}^{2+}/\text{Ni}^{3+}$ redox features become more prominent with each CV cycle (Supplementary Fig. 10). The non-iR-corrected CV data are presented in Supplementary Fig. 10d. The observed variations in peak shifts and disparities in OER performance, especially with minimal Fe incorporation, underscore the critical role of electrolytic Fe in enhancing active sites and boosting OER activity. Consistent with these results, 50 h EA operation with the varying electrolyte conditions showed increasing promotion effects with increasing Fe contents within the electrolytes (Fig. 3b and Supplementary Fig. 11). In the unpurified KOH electrolyte, the overpotential at 0.5 A cm^{-2} decreased by $274 \pm 8 \text{ mV}$ following 50 h of EA operation. Conversely, in 99.99% and purified KOH electrolytes, the overpotentials at 0.5 A cm^{-2} decreased by 203 ± 22 and $32 \pm 12 \text{ mV}$, respectively. Exogenous addition of 100 ppm Fe (Fe-KOH) also increased the OER activity upon EA operation, although to a lesser extent, presumably due to overriding initial activation effects (Supplementary Fig. 12). The limited reactivation of NF observed in Fe-KOH can be explained by reduced Fe

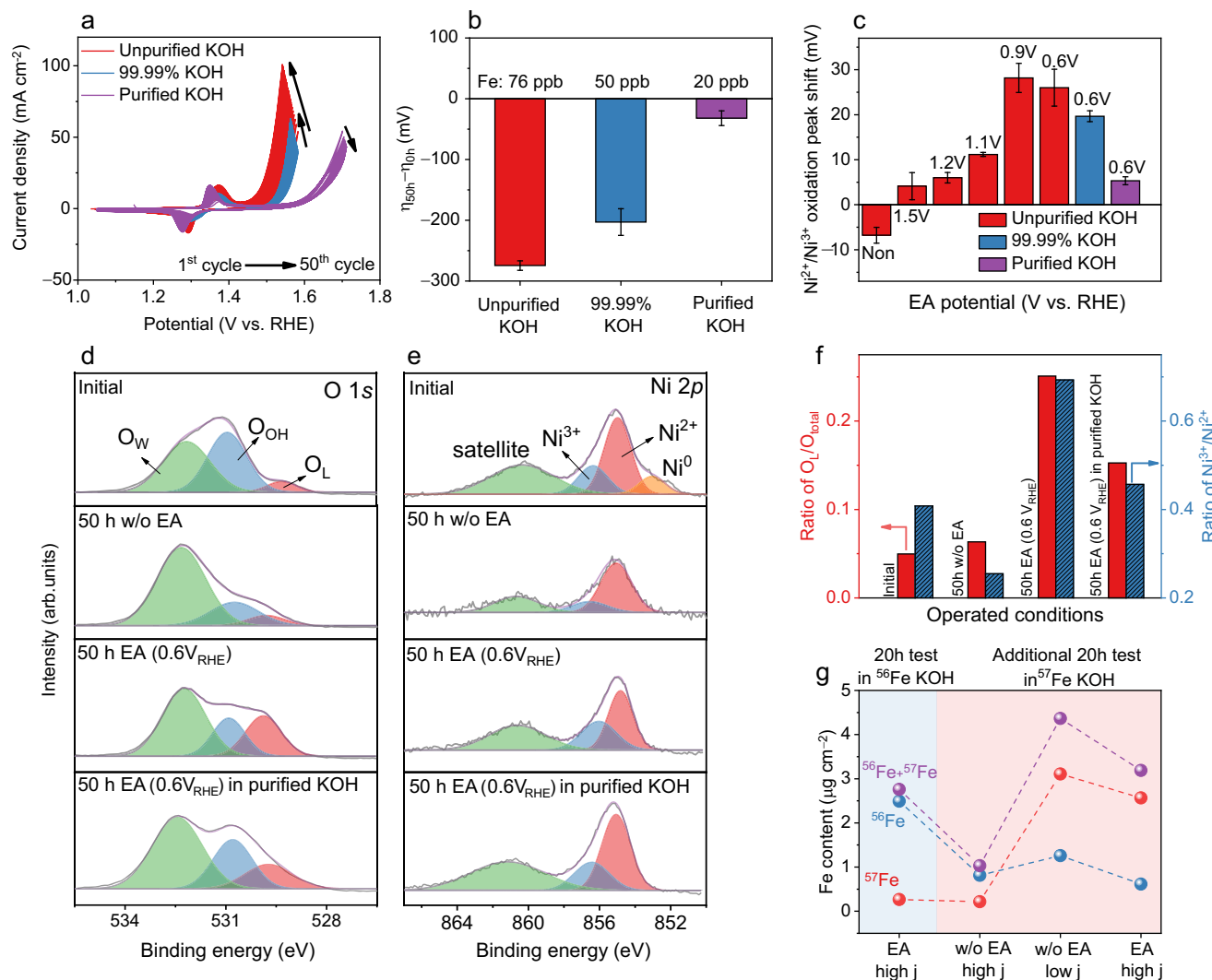


Fig. 3 | The role of Fe in EA operation. **a** CV scans of NF in an unpurified KOH solution (Fe: 76 ppb), a 99.99% KOH solution (Fe: 50 ppb), and a purified KOH solution (Fe: 20 ppb) with a scan rate of 20 mV s⁻¹. The pH value of each electrolyte was 14. **b** Overpotential difference between before (η_{0h}) and after (η_{50h}) 50 h of EA operation with varying Fe concentrations in 1 M KOH solutions. **c** Comparison of the α -Ni(OH)₂/γ-NiOOH oxidation peak shift before and after various EA operations for 50 h. A positive value indicates an anodic shift after 50 h compared to the initial state. XPS **(d)** O 1s and **(e)** Ni 2p spectra of NF before and after various EA

operations. **f** Ratios of O_L/O_{total} and Ni^{3+}/Ni^{2+} before and after various EA operations, which were determined by comparing XPS peak areas. **g** The total Fe content in NF after various operation conditions. The EA operation with 0.6 V_{RHE} was first carried out for 20 h in unpurified KOH containing a natural isotopic abundance of ⁵⁶Fe and ⁵⁷Fe. Subsequently, a second 20 h experiment was conducted in purified KOH with the addition of 100 ppb ⁵⁷Fe, operating under either high (0.5 A cm⁻²) or low current density (30 mA cm⁻²) conditions with or without the EA protocol. Error bars indicate standard errors obtained from 3 independent replicates.

dissolution in net, along with the surplus Fe in electrolyte facilitating Fe incorporation.

The impact of Fe incorporation was scrutinized using diverse electrochemical and materials characterization techniques. During CV cycling, the α -Ni(OH)₂/γ-NiOOH oxidation peak showed an anodic shift in unpurified KOH, contrasting with a cathodic shift in purified KOH (Fig. 3a and Supplementary Fig. 10). This shift is attributed to a partial charge transfer effect from Fe incorporation, which impedes the oxidation of Ni²⁺^{33,38,43}. We have detailed the extent of oxidation peak shifts of α -Ni(OH)₂/γ-NiOOH after 50 h of operation compared to its initial state under various EA potentials and KOH electrolyte conditions in Fig. 3c (Supplementary Fig. 6 and Supplementary Fig. 13). Notably, the most substantial anodic shift, 28 ± 3 mV, occurred in the unpurified KOH solution when EA was applied at 0.6 and 0.9 V_{RHE}, highlighting the pronounced effect of EA on Fe incorporation. X-ray photoelectron spectroscopy (XPS) analysis further corroborates the observed trend. Using peak deconvolutions of O 1s and Ni 2p spectra recorded under various conditions, we tracked changes in the relative

intensity of lattice oxygen (O_L/O_{total}) and the ratio of Ni³⁺ to Ni²⁺ (Ni^{3+}/Ni^{2+}), which are proportional to the amount of surface NiOOH phase^{44,45}. For this quantitative analysis, we conducted deconvolution of O 1s spectra into lattice oxygen (O_L , -529.7 eV), hydroxyl (O_{OH} , -531.2 eV), and chemisorbed water (O_W , -532.4 eV)^{46–48} (Fig. 3d) and Ni 2p spectra into Ni²⁺ (-855.3 eV), Ni³⁺ (-856.8 eV), and satellite (-861.6 eV)^{22,49} (Fig. 3e). Among the various conditions tested, 50 h EA (0.6 V_{RHE}) in the unpurified KOH resulted in the highest O_L/O_{total} and Ni^{3+}/Ni^{2+} values of 0.25 and 0.69, respectively (Fig. 3f), indicating the critical roles of Fe and EA protocol in promoting the formation of the NiOOH phase for active OER. Additionally, in situ Raman spectra show that 50 h EA (0.6 V_{RHE}) has a higher peak intensity ratio of 557 cm⁻¹ to 480 cm⁻¹ (I_{557}/I_{480}) of 0.84 compared to 0.81 in 50 h w/o EA (Fig. 2e), indicating greater structural disorder owing to Fe incorporation^{43,50–52}. X-ray diffraction (XRD) analysis also reveals that 50 h EA (0.6 V_{RHE}) shows the most significant peak shift and phase separation of the Ni (111) and Ni (200) facets, indicating the pronounced structural disorder (Supplementary Fig. 14).

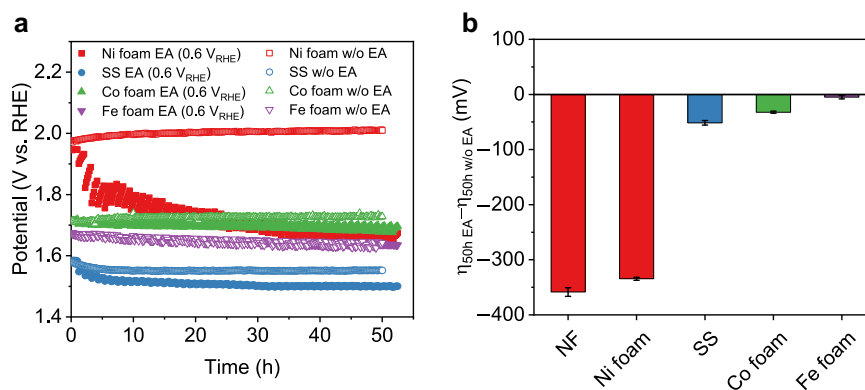


Fig. 4 | EA operation with other electrodes. **a** Potential traces of Ni foam, SS felt, Co foam, and Fe foam at 0.5 A cm^{-2} with and w/o EA operation in unpurified 1 M KOH solutions. **b** Overpotential difference at 0.5 A cm^{-2} after 50 h between

operations with ($\eta_{50h\ EA}$) and w/o EA ($\eta_{50h\ w/o\ EA}$). Error bars indicate standard errors obtained from 3 or more independent replicates.

Although the incorporated Fe was barely detected by XPS and scanning electron microscope-energy dispersive X-ray spectroscopy (SEM-EDS), due to the overriding bulk characteristics of the NF (Supplementary Figs. 15–18, Supplementary Table 1 and Supplementary Table 2), ICP-MS analysis enabled the quantification of the incorporated Fe. To investigate the dynamic interaction between electrolytic Fe species and NF under EA conditions, we utilized Fe isotopes. The initial EA was performed at $0.6\text{ V}_{\text{RHE}}$ for 20 h using unpurified KOH containing a natural isotopic abundance of ^{56}Fe and ^{57}Fe (Fig. 3g, blue area). This was followed by a subsequent operation for 20 h in purified KOH supplemented with 100 ppb of ^{57}Fe , conducted under either high current density (0.5 A cm^{-2}) or low current density (30 mA cm^{-2}) (Fig. 3g, red area). Initially, the NF incorporated approximately $2.5\text{ }\mu\text{g cm}^{-2}$ of ^{56}Fe after 20 h of EA operation in unpurified KOH. However, after 20 h of operation at 0.5 A cm^{-2} w/o EA, the total Fe content decreased to about $1\text{ }\mu\text{g cm}^{-2}$, indicating substantial Fe dissolution under high current density conditions. This loss was significantly mitigated when operations were conducted at low current density or under continued EA at high current density, where the total Fe content increased to about $4.4\text{ }\mu\text{g cm}^{-2}$ and $3.2\text{ }\mu\text{g cm}^{-2}$, respectively. Furthermore, under both conditions, the ^{56}Fe content was found to be 2–3 times greater than that of ^{57}Fe , demonstrating a dynamic exchange of Fe between the NF and the electrolyte. Further quantification after 50 h of EA at $0.6\text{ V}_{\text{RHE}}$ under high current density revealed that the Fe content in NF reached $5.5 \pm 1.3\text{ }\mu\text{g cm}^{-2}$, which is about 2.3 and 1.5 times higher than the levels observed without EA and under EA at $1.2\text{ V}_{\text{RHE}}$, respectively (Supplementary Fig. 19). When conducted in purified KOH under the same EA conditions, Fe incorporation was about 2.2 times lower. These results indicate that the EA protocol maintains high OER activity under high current densities by dynamically re-depositing electrolytic Fe ions onto NF.

In summary, our combined electrochemical and material characterization reveals that Fe in NF undergoes dissolution under high current density conditions, followed by redeposition during EA, leading to enhanced OER performance. By systematically tuning the Fe^{3+} concentration in the KOH electrolyte and the applied EA potential, we found that effective activation occurs when the Fe^{3+} concentration exceeds $\sim 76\text{ ppb}$ and a periodic reductive potential below $1.1\text{ V}_{\text{RHE}}$ is applied. The incorporation of Fe is corroborated by CV peak shifts, Raman spectroscopy, XRD, and ICP-MS. Moreover, the EA protocol preferentially promotes the formation of $\gamma\text{-NiOOH}$ phases, as confirmed by CV, in situ Raman, and X-ray photoelectron spectroscopy (XPS), indicating that Fe-incorporated $\gamma\text{-NiOOH}$ serves as the catalytically active phase responsible for the improved OER activity. This mechanistic insight establishes that the intermittent application of reductive potentials drives dynamic regeneration of active sites and

catalyst healing, in contrast to previous strategies that rely on irreversible surface reconstruction under static polarization conditions^{53–55}.

EA operation with other electrodes

We applied the same EA protocol to other readily available metal electrodes, including Ni foam, stainless steel felt (SS), Co foam, and Fe foam. Among other electrodes, Ni foam exhibited the most notable activation and reactivation with the EA operation, showing a $335 \pm 3\text{ mV}$ decrease in overpotential at 0.5 A cm^{-2} compared to normal operation w/o EA (Fig. 4a, red). Similar to NF, Ni foam also experienced the selective emergence of the $\gamma\text{-NiOOH}$ phase during EA (Supplementary Fig. 20), suggesting that the same mechanism for NF activation is generally operative in Ni foam. Additionally, we tested NF with varying thickness and porosity, as well as Ni mesh and Ni foil, to assess the effect of EA operation (Supplementary Fig. 21). The results confirmed that EA operation significantly enhances the OER performance across all Ni-based electrodes. The same EA protocol also resulted in non-negligible activation effects on other electrodes, such as SS felt and Co foam, reducing overpotential by 52 ± 4 and $32 \pm 2\text{ mV}$ at 0.5 A cm^{-2} , respectively (Fig. 4b and Supplementary Fig. 22). The lack of significant performance improvement under a more reductive environment during the EA process on the SS felt suggests that, consistent with the mechanism identified in NF, Fe redeposition does not require a potential below $0.6\text{ V}_{\text{RHE}}$ (Supplementary Fig. 23). We synthesized a NiFe alloy catalyst on NF via electrodeposition and conducted EA operation. While the NiFe catalyst initially exhibited high OER performance, its activity declined under EA conditions (Supplementary Fig. 24). After 50 h, the NiFe-based catalyst showed only a $\sim 40\text{ mV}$ difference in overpotential compared to the EA-treated NF at 500 mA cm^{-2} . These results suggest that EA operation accelerates the degradation of pre-coated catalysts and that bare NF under EA conditions can achieve comparable performance to NiFe-based catalysts.

Following the Fe adsorption energy trends for Ni, Co, and Fe hydr(oxy)oxide electrodes¹, we speculate that Fe plays a more dramatic role in gating the structural dynamics of Ni-based electrodes, giving rise to the most pronounced activation effect during our EA protocol. Without desirable active site/host interactions, Co and Fe foam would not form dynamically stable OER interfaces, and thus, dynamic polarization effects may not be pronounced as compared to Ni-based electrodes¹. While a detailed analysis of structural changes and Fe insertion was not conducted, the observed results offer preliminary evidence suggesting a correlation between the enhanced OER performance from EA operation and the Fe adsorption energy on the host material. Considering the vastly different (re)activation magnitudes observed in Ni, Co, and Fe foams despite their similar

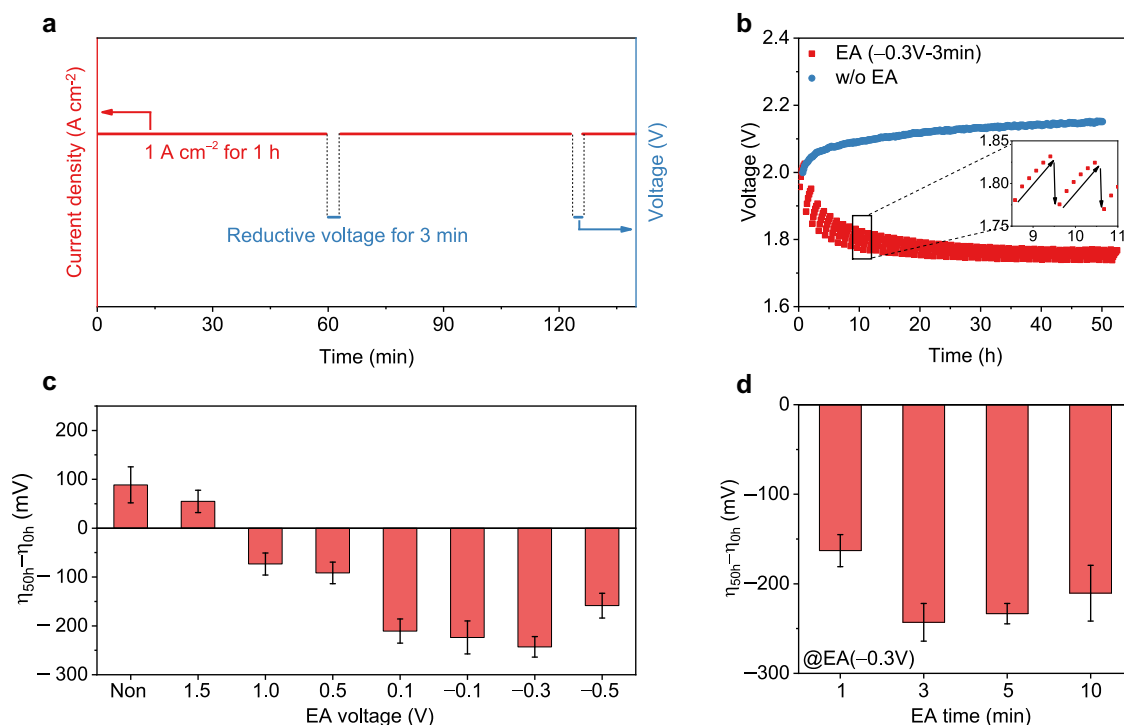


Fig. 5 | EA operation in the AEMWE single-cell system. **a** EA conditions for the AEMWE single-cell system. **b** Cell voltage traces at 1 A cm^{-2} with and w/o EA operation in the unpurified 1 M KOH solution at 60°C using the NF anode and Pt/C cathode. The black arrow in **(b)** indicates the sequence of this data collection. **c** Overvoltage difference before and after 50 h EA operation with varying reductive

activating voltages. **d** Overvoltage difference before and after 50 h EA operation with a transient reductive voltage of -0.3 V with a time variable. All reported voltages are presented without iR compensation. Error bars indicate standard errors obtained from 3 or more independent replicates.

morphologies and the same currents applied, we posit that the potential mitigation of concentration polarization or local pH swing effects upon EA operation is not significant.

Scale-up feasibility

We applied our EA protocol to the AEMWE single-cell system, comprising the NF anode, a platinum on carbon (Pt/C) cathode, and an HQPC-TMA membrane⁵⁶. This system was operated in the unpurified 1 M KOH solution at 60°C for 50 h. The EA procedure involved repeating a sequence of chronopotentiometry at 1 A cm^{-2} for 1 h followed by chronoamperometry at varying activating voltages for 3 min (Fig. 5a). Unlike the three-electrode half-cell system, the two-electrode AEMWE system was optimized for EA operation using voltage as the control variable rather than potential. The most significant performance enhancement was observed when the activating voltage was set at -0.3 V (Fig. 5c, Supplementary Fig. 25, and Supplementary Fig. 26) for 3 min (Fig. 5d, Supplementary Fig. 27, and Supplementary Fig. 28) during EA operation. The application of the activating voltage in this protocol led to negative current decays starting from approximately -10 mA cm^{-2} to nearly zero within 3 min (Supplementary Fig. 26f), consistent with the observations from the above half-cell studies. Compared to the $90 \pm 37 \text{ mV}$ increase in cell voltage after 50 h of constant 1 A cm^{-2} water electrolysis w/o EA, the optimized EA operation with -0.3 V activating for 3 min (-0.3 V -3 min) resulted in a decrease in cell voltage by $243 \pm 21 \text{ mV}$ (Fig. 5b). After 50 h of operation, the optimized EA operation achieved over 10% higher system efficiency ($71 \pm 1\%$) compared to the w/o EA system ($60 \pm 1\%$) and exhibited a Faradaic efficiency of $99 \pm 1\%$ (Supplementary Fig. 29). Consistent with the half-cell analyses, the activation and reactivation features were commonly observed in this single-cell operation (black arrow in Fig. 5b). This voltage fluctuation arises from Fe migration between the electrolyte and NF, contributing to performance enhancement rather than system degradation. In situ EIS analysis

revealed a decrease of $-0.03 \Omega \text{ cm}^2$ in ohmic resistance and $0.13 \Omega \text{ cm}^2$ in charge transfer resistance over the first 20 h, indicating that the primary factor behind the performance improvement was the enhanced OER kinetics due to Fe incorporation (Supplementary Fig. 30). The optimized EA protocol demonstrated significant performance enhancements in $1 \text{ M K}_2\text{CO}_3$ and pure water containing 100 ppb of Fe, as well as in unpurified KOH at a current density of 4 A cm^{-2} (Supplementary Fig. 31). Although there was an initial performance boost, a gradual decline was observed over time due to the harsh operational conditions. The EA operation in the Fe-KOH solution (1 M KOH containing 100 ppm Fe) resulted in inferior performance relative to the system without additional Fe, likely due to membrane degradation caused by excess Fe^{22,57}. We also conducted EA operations under optimized conditions in dry cathode mode (Supplementary Fig. 32). The results from this configuration demonstrated a reduction in cell voltage comparable to that observed under normal operational conditions, highlighting the general applicability of our EA protocol.

Equipped with the established protocols for single-cell configurations, we conducted a long-term EA operation (Fig. 6a and Supplementary Fig. 33). For EA operation using a commercial membrane (X37-50 Grade RT), the starting cell voltage of 2.1 V was reduced to 1.8 V during the initial 50 h, consistent with the above results. After 50 h, however, the single cell experienced a gradual increase in cell voltage and reached -1.9 V at 525 h. During this period, the high-frequency resistance (HFR) rose from $-0.08 \Omega \text{ cm}^2$ to $0.14 \Omega \text{ cm}^2$. Conversely, the resistance represented by the EIS semicircle decreased (Fig. 6b, blue). Thus, the observed performance loss is presumably due to the deterioration of the membrane rather than degradation at the catalytic interfaces. Fourier transform-infrared spectroscopy (FT-IR) and time-of-flight secondary ion mass spectroscopy (ToF-SIMS) analysis of the commercial membrane after use revealed a substantial reduction in its cationic groups ($\sim 20\%$) (Supplementary Figs. 34–38). More evidently, when the experiment resumed after 525 h by replacing

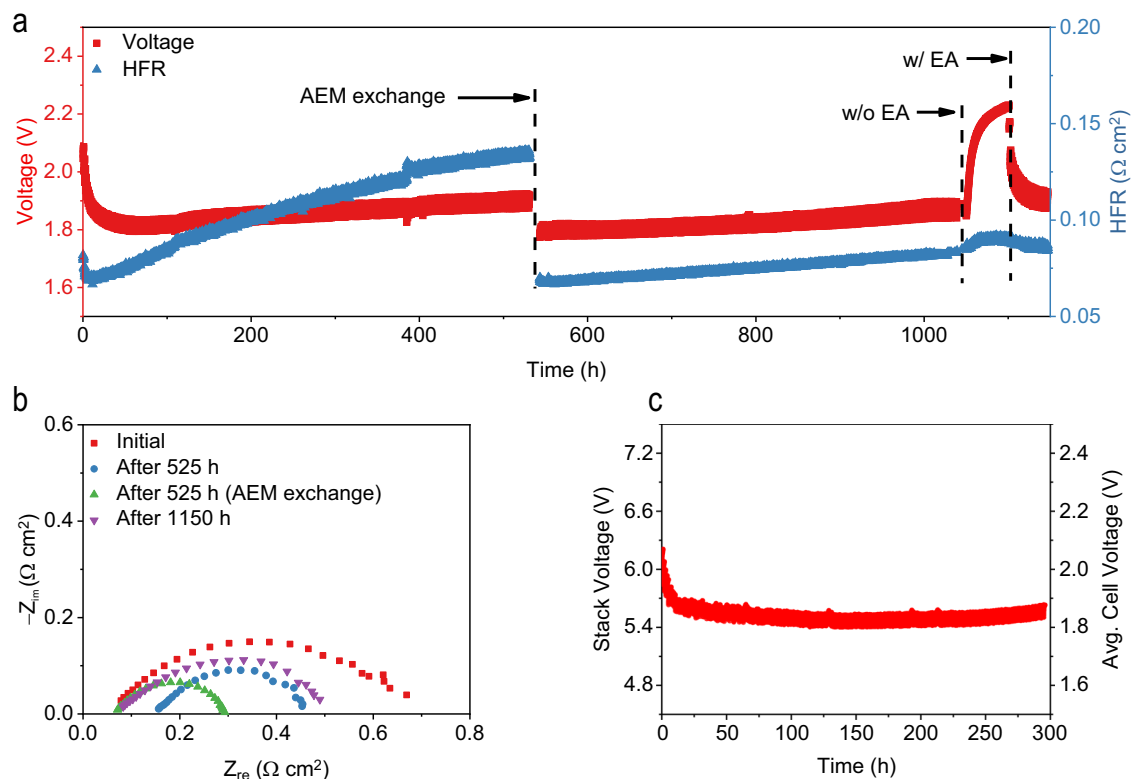


Fig. 6 | Scale-up feasibility in the long-term EA operation. **a** Cell voltage and HFR traces at 1 A cm^{-2} during the long-term EA operation in 1 M KOH at 60°C . The X37-50 Grade RT membrane was used for 525 h and subsequently replaced with the HQPC-TMA membrane without changing the electrodes. The EA operation was

conducted from 0 to 1050 h, paused between 1050 and 1100 h, and resumed at 1100 h. **b** EIS plots for the AEMWE system over time. **c** Stack voltage and average cell voltage traces at 1 A cm^{-2} in the 3-cell stack AEMWE system during 300 h of EA operation. All reported voltages are presented without iR compensation.

the aged membrane with the state-of-the-art HQPC-TMA under otherwise identical conditions, the cell voltage and the HFR values immediately decreased to $\sim 1.78 \text{ V}$ and $0.07 \Omega \text{ cm}^2$, respectively, thus corroborating the deterioration of the commercial membrane rather than the degradation of catalytic interfaces. The compatibility between the HQPC-TMA membrane and our EA protocol resulted in relatively low increases in cell voltage ($\sim 50 \text{ mV}$) and HFR ($\sim 12 \text{ m}\Omega \text{ cm}^2$). Consistently, ex-situ FT-IR and ToF-SIMS analysis of the used HQPC-TMA membrane showed only a 2% reduction in its cationic groups after 525 h EA operation (Supplementary Figs. 34–38). The cationic group loss, along with other degradation factors such as local pH variations, CO_2 dissolution, and interfacial issues, may contribute to the observed HFR increase.

The feasibility of our EA protocol is further highlighted by the sequential off-on experiment: when the EA operation was off (at 1050 h), the cell voltage experienced an immediate surge to $\sim 2.2 \text{ V}$, which again decreased to $\sim 1.9 \text{ V}$ upon resumption of EA operation. Due to the severe catalyst degradation during the operation w/o EA from 1050 to 1100 h, the cell voltage at 1150 h was $\sim 60 \text{ mV}$ higher than at 1050 h, leading to an increase in the charge transfer resistance (Fig. 6b, purple). This interpretation is further corroborated by the linear sweep voltammetry (LSV) curves obtained over time (Supplementary Fig. 39). The Pt/C catalyst maintained its structural integrity after prolonged operation, showing no significant changes in XRD patterns (Supplementary Fig. 40a). Additionally, the catalyst demonstrated stable hydrogen evolution performance during a 50 h EA operation in a half-cell system, indicating minimal disturbance from the Pt/C cathode during EA operation (Supplementary Fig. 40b).

The scalability of our approach is further validated through a 25 cm^2 three-cell stack AEMWE, employing bare NF as the anode and a HQPC-TMA membrane. Under EA operation, the system maintains a

stable cell voltage of $\sim 1.8 \text{ V}$ over 300 h (Fig. 6c, Supplementary Figs. 41 and 42), demonstrating durable performance under practical conditions. This seamless translation from half-cell optimization to a multi-cell electrolyzer highlights the robustness of the EA protocol, which is specifically tailored for simple, commercially available electrode configurations. Our study systematically quantifies and mechanistically elucidates the processes of Fe dissolution, redeposition, and stabilization during EA. We uncover how Fe incorporation dynamically modulates the phase evolution of NiOOH, enabling the formation and persistence of catalytically active states even under high current density conditions—a regime previously underexplored. In contrast to earlier studies that primarily focus on short-term half-cell performance at low current densities, we extend the operational window to sustained, full-cell electrolysis at industrially relevant conditions. Altogether, these findings establish a scalable and mechanistically grounded framework for Fe-mediated catalyst activation, bridging fundamental electrochemical principles with practical implementation in large-scale water electrolysis systems.

Discussion

In this study, we establish a dynamic polarization strategy as a robust and scalable approach to enhance the performance of Ni-based electrodes for OER under alkaline conditions. By systematically implementing an EA protocol—featuring the periodic application of reductive potentials—we enable continuous regeneration of catalytically active Fe-incorporated $\gamma\text{-NiOOH}$ phases on readily available Ni electrodes. Our findings reveal that precise control over Fe^{3+} concentration in the electrolyte, combined with appropriate EA potentials, is critical to modulating interfacial redox chemistry and sustaining high OER activity. Comprehensive spectroscopic and structural analyses confirm that the dynamic polarization environment not only

facilitates Fe redeposition but also stabilizes OER-active surface phases, offering a mechanistic framework for catalyst self-healing during extended operation. This redox-driven regeneration strategy enables gradual yet durable activation of the electrode surface, distinguishing it from conventional static reconstruction approaches. Importantly, the performance gains achieved at the half-cell level directly translate to practical systems. The EA protocol supports stable operation of an AEMWE at 1 A cm^{-2} with a cell voltage of -1.8 V for over 1000 h using bare NF anodes. Furthermore, the strategy proves scalable, with a 25 cm^2 three-cell AEMWE stack maintaining performance over 300 h with negligible voltage loss—demonstrating its viability for real-world deployment. Taken together, our work introduces a generalizable framework for dynamically modulating the OER interface to maintain catalyst activity and structural integrity under industrially relevant conditions. This approach offers a compelling complement to chemical design strategies and opens new directions for achieving long-term, scalable water electrolysis using earth-abundant electrode materials. By bridging mechanistic insight with device-level validation, the dynamic polarization strategy holds promise for accelerating the development of next-generation electrolyzer technologies.

Methods electrochemical measurements in half-cell systems

Electrochemical tests were performed in undivided cells using an SP-150 potentiostat (Biologic) with a saturated calomel electrode (SCE, CHI150, Quins) as a reference electrode and Pt foil (Pt/Ti electrode, Wescor Electrode) as a counter electrode. All electrolyte solutions, except for 99.99% KOH and purified KOH, which were stored in polypropylene bottles, were prepared prior to the electrochemical experiments and stored in glass bottles. All electrochemical half-cell experiments were conducted in an H-type cell, with 50 mL of electrolyte in both the anode and cathode compartments (Fig S43a). Before the experiments, all components of the electrochemical cell underwent cleaning with $1\text{ M H}_2\text{SO}_4$ (which was fabricated by H_2SO_4 95–97%, Sigma-Aldrich) and thorough rinsing with pure-water ($18.2\text{ M}\Omega\text{-cm}$, Milli-Q® Direct 8 system, Merck Millipore, MA, USA). Pt counter electrodes were cleaned with aqua regia before and after the experiment. Before and after the experiments, we calibrated the potential of the SCE through CV tests employing $[\text{Fe}(\text{CN})_6]^{4-}/[\text{Fe}(\text{CN})_6]^{3-}$. The SCE calibration test was conducted in a solution containing 5 mM potassium ferricyanide (III) (99%, Sigma-Aldrich), 5 mM potassium hexacyanoferrate (II) trihydrate (98.5–102.0%, Sigma-Aldrich), and 0.5 M KCl (99%, Sigma-Aldrich). All potentials were measured with respect to the SCE and converted to the RHE scale using the equation: $E_{\text{RHE}} = E_{\text{SCE}} + (0.059\text{ V} \times \text{pH})$. The bare NF (thickness = $250\text{ }\mu\text{m}$, porosity = 60%, and fiber diameter = $20\text{ }\mu\text{m}$; 2Ni18-025, Bekaert) was used as a working electrode. The geometric surface area of the working electrode was 1 cm^2 . In EA operation, the NF was cycled between a current density of 0.5 A cm^{-2} for 1 h and a set potential (1.5, 1.2, 1.1, 0.9, or $0.6\text{ V}_{\text{RHE}}$) for 3 min, repeated 50 times. During the EA operation, the potential and HFR of NF at 0.5 A cm^{-2} were measured every 10 min, and current density at a set potential was measured every 1 min. CV measurements were conducted with a scan rate of 20 mV s^{-1} within the potential range of -1 – $1.6\text{ V}_{\text{RHE}}$ before and after the EA operation. To determine the double layer capacitance (C_{dl}) values of the catalysts, CV measurements spanned approximately 0.7 – $0.8\text{ V}_{\text{RHE}}$ with scan rates of 20, 40, 60, 80, and 100 mV s^{-1} . Specifically, the ECSA with C_{dl} values was determined from the slope of the linear plot of half of the difference between the oxidation and reduction current densities at $0.76\text{ V}_{\text{RHE}}$ versus the scan rate. Unless noted, all electrochemical experiment data were iR-corrected, addressing the ohmic resistance measured via EIS at 50 KHz with a 10 mV amplitude. The iR correction was conducted based on the ohmic resistance values determined from the x-intercepts of the Nyquist plots. The preparation of a 1 M KOH solution varied according to the experimental conditions, utilizing either KOH (90%, Sigma-Aldrich), KOH (99.99%, Sigma-Aldrich), or purified

KOH. All 1 M KOH solutions exhibited a pH of 14 ± 0.2 . Ni foam (EQ-bcnf-1.6 mm, MTIKorea), SS (10AL3, Bekaert), Co foam (EQ-CoF-1110, MTIKorea), and Fe foam (SP1257, Sinopro) were also tested as working electrodes after being pressed to approximately $300\text{ }\mu\text{m}$. The NF ($400\text{ }\mu\text{m}$ with porosities of 50%, 70%, and 80%, Alantum), Ni mesh ($100\text{ }\mu\text{m}$ mesh woven from 0.1 mm dia wire, Thermo Scientific Chemicals), and Ni foil (0.25 mm thick, annealed, 99.5%, Thermo Scientific Chemicals) were also tested for EA operation. The NiFe-based catalyst was fabricated via electrodeposition on the NF electrode. Electrodeposition was performed using the NF as the working electrode, Pt foil as the counter electrode, and SCE as the reference electrode. The NF underwent electrodeposition at $-0.95\text{ V}_{\text{SCE}}$ for 5 min in a solution of 30 mM $\text{NiCl}_2 \cdot 6\text{H}_2\text{O}$ (99.9%, Sigma-Aldrich) + 30 mM $\text{FeCl}_3 \cdot 6\text{H}_2\text{O}$ (97%, Sigma-Aldrich). Subsequently, the electrode underwent a water rinse and was dried at 40°C for more than 20 min.

Fe isotope experiments

To quantitatively analyze the dynamic interaction between electrolytic Fe and NF, an initial EA operation was conducted in unpurified KOH at 500 mA cm^{-2} and $0.6\text{ V}_{\text{RHE}}$ for 20 h. Following this process, the NF was immersed in a 100 ppb ^{57}Fe solution prepared in the purified KOH for further testing. The 100 ppb ^{57}Fe solution was prepared by precisely diluting a ^{57}Fe standard solution (Iron 57, plasma standard solution, Specpure™, ^{57}Fe $10\text{ }\mu\text{g mL}^{-1}$, Thermo Scientific Chemicals) into the purified KOH to achieve a final concentration of 100 ppb. The experiment was performed under three conditions: (i) w/o EA at high current density (500 mA cm^{-2}), (ii) w/o EA at low current density (30 mA cm^{-2}), and (iii) with EA at 500 mA cm^{-2} and $0.6\text{ V}_{\text{RHE}}$, each for 20 h. After the tests, the NF samples were thoroughly rinsed with pure-water and subsequently analyzed using ICP-MS.

Electrolyte purification

The KOH electrolyte purification to adjust the Fe concentration was conducted by precipitation method using $\text{Ni}(\text{NO}_3)_2 \cdot 6\text{H}_2\text{O}$ (99.9%, Sigma-Aldrich)^{34,38}. 2 g of $\text{Ni}(\text{NO}_3)_2 \cdot 6\text{H}_2\text{O}$ was dissolved in 4 mL of pure water in a 50 mL polypropylene centrifuge tube. After vigorous mixing, 20 mL of 1 M unpurified KOH electrolyte was added, leading to $\text{Ni}(\text{OH})_2$ precipitation. The tube was subjected to sonication in an ultrasonic bath for 10 min and centrifuged at 8000 rpm for 10 min, followed by careful decantation of the supernatant. This process was iterated three times, involving the addition of 20 mL of pure water and 2 mL of KOH electrolyte, sonication, centrifugation, and decantation of the supernatant. Subsequently, the precipitate underwent three sequential rinses with 5 mL of KOH electrolyte, followed by an addition of 30 mL of KOH electrolyte. After two cycles of redispersion with vortex mixing and sonification, 20 mL of KOH electrolyte was added and left to settle for at least 50 h. After centrifugation (10,000 rpm, 10 min) and decantation, the supernatant was filtered with a polyvinylidene fluoride membrane filter ($0.45\text{ }\mu\text{m}$, Sigma-Aldrich) and stored in a clean polypropylene bottle.

Material characterization

In situ Raman spectra were obtained using a confocal Raman microscope (HEDA, NOST) with a light source of 532 nm, under applied potentials ranging from 0.6 to $1.7\text{ V}_{\text{RHE}}$. For precise analysis, each spectrum was obtained at least three times. For the in situ set-up, a Pt foil served as the counter electrode, while a SCE was selected as the reference electrode (Fig S43b). Each spectrum was calibrated using the silicon Raman peak at 520.8 cm^{-1} . XPS analysis was performed utilizing an AXIS Supra (Kratos, UK) at the National Center for Inter-university Research Facilities (NCIRF) at Seoul National University (SNU). The Fe contents in the KOH solutions and NF were measured via ICP-MS with the Agilent 7900 system. SEM and EDS analyses were performed using a JSM-7800F Prime instrument (JEOL, Japan), operated at a 15 kV accelerating voltage at the NCIRF at SNU. XRD analysis was performed

employing a SmartLab system (Rigaku, Japan) with Cu K α radiation (40 kV, 250 mA) within the 2 θ range of 20°–70°, utilizing a scan speed of 3° s^{−1}.

Electrochemical evaluation in the AEMWE single-cell systems

In the AEMWE single-cell test, the NF anode and Pt/C cathode catalysts (1 cm²) were utilized, along with Au-coated Ti flow fields and end plates provided by CNL Energy company. The NF anode was used without any pretreatment. The Pt/C electrode, with a loading of 1 mg cm^{−2} on carbon paper (10 BC, Sigracet), was fabricated via the spraying-coating technique. The cathode ink slurry, comprising 0.16 g of Pt/C powder (47 wt%, Tanaka K.K.), 0.8 g of 5 wt% XB-7 ionomer (Dioxide Materials), 3 g of water, and 9.2 g of isopropyl alcohol, was subjected to 1 h of sonication prior to spray coating for 30.25 cm² of carbon paper. After allowing the electrolyte to dry completely following each spray, the weight was measured using an electronic scale. Spraying was repeated until the mass of Pt, excluding the carbon and ionomer, reached 1 mg cm^{−2}. For AEMs, HQPC-TMA-2.4 (thickness: 30 μ m)⁵⁶ and X37-50 Grade RT (thickness: 50 μ m, Dioxide Materials) were used according to the experimental conditions, which were stored in 1 M KOH for 24 h before usage. In the AEMWE test, the AEM was used in a size of 1.5 \times 1.5 cm². In the AEMWE system, the unpurified 1 M KOH solution circulated both the cathode and anode at a flow rate of 30 mL min^{−1}, while being held at 60 °C. In EA operation, the single-cell system was cycled between a current density of 1 A cm^{−2} for 1 h and a set voltage (1.5, 1.0, 0.5, 0.1, −0.1, −0.3, or −0.5 V) for 3 min, repeated 50 times. During the EA operation, the cell voltage and HFR of the system at 1 A cm^{−2} were measured every 10 min, and current density at a set voltage was measured every 1 min. The HFR was measured during the EA operation via the EIS technique at 50 KHz with a 10 mV amplitude. Before and after the long-term EA operation, EIS measurements were conducted at a cell voltage of 1.6 V, spanning from 50 KHz to 1 Hz with a 10 mV amplitude. The AEMWE system efficiency was determined using Eq. 1.

$$\text{system efficiency} = \frac{H_2 \text{ power out}}{AEMWE \text{ power}} \times 100\% \quad (1)$$

The H₂ power out was calculated by multiplying the hydrogen production rate (5.18 $\times 10^{-6}$ mol H₂ cm^{−2}s^{−1} at 1 A cm^{−2}) and a lower heating value of H₂ (242,000 J mol^{−1}). The power of the AEMWE system was calculated by multiplying a current density of 1 A cm^{−2} and the cell voltage. For the Faradaic efficiency, we measured the volume of the generated O₂ using the water–gas displacement method at 1 A cm^{−2} and compared it with the theoretical value. The Faradaic efficiency was calculated using Eq. 2:

$$\text{Faradaic efficiency} = \frac{nF \times m}{Q} \quad (2)$$

where n denotes the number of electrons ($n=4$) involved per O₂ molecule generated, F is the Faraday constant (96485 C mol^{−1}), m is the number of moles of generated O₂, and Q is the total charge passed.

Electrochemical evaluation in the 3-cell stack AEMWE system

The 3-cell stack with an active area of 25 cm² was assembled using customized cell hardware fabricated by CNL Energy company. The stack components included graphite-coated alumina end plates, Pt-coated Ti-based bipolar plates, and Au-coated current collectors (Supplementary Fig. 41a). Before stack assembly, HQPC-TMA-2.4 membranes with a thickness of 30 μ m were pretreated by soaking them in 1 M KOH solution for 24 h and then washing them with deionized water. Each hydroxide form of the membranes was then sandwiched between two porous transport electrodes with PTFE-film gaskets (260 μ m for the anode and 220 μ m for the cathode). Bare NF

with dimensions of 5 \times 5 cm² was used for the anode, while Pt/C-coated carbon paper (10 BC, Sigracet) with dimensions of 5.2 \times 5.2 cm² was used for the cathode. The Pt loading in the cathode was 1 mg cm^{−2} and the same catalyst slurry as in the single-cell test was used for the cathode fabrication. The assembled 3-cell stack (Supplementary Fig. 41b) was integrated into an AEMWE test station fabricated by CNL Energy company. After that, 1 M KOH solution was circulated through the stack at a temperature of 60 °C with a flow rate of 50 mL min^{−1} for 1 h. Following this pre-conditioning step, the stack was cyclically operated between a current density of 1 A cm^{−2} for 1 h and a current density of −5 mA cm^{−2} for 3 min for EA operation. All the electrochemical tests on the 3-cell stack were conducted using a potentiostat (HCP-803, Biologic).

Data availability

All data generated and analyzed in this study are included in the article and Supplementary Information. Source data are provided with this paper.

References

- Chung, D. Y. et al. Dynamic stability of active sites in hydr(oxy) oxides for the oxygen evolution reaction. *Nat. Energy* **5**, 222–230 (2020).
- Haase, F. T. et al. Size effects and active state formation of cobalt oxide nanoparticles during the oxygen evolution reaction. *Nat. Energy* **7**, 765–773 (2022).
- Li, A. et al. Enhancing the stability of cobalt spinel oxide towards sustainable oxygen evolution in acid. *Nat. Catal.* **5**, 109–118 (2022).
- Razmjooei, F. et al. Increasing the performance of an anion-exchange membrane electrolyzer operating in pure water with a nickel-based microporous layer. *Joule* **5**, 1776–1799 (2021).
- Kim, M. G. et al. Realizing the potential of hydrophobic crystalline carbon as a support for oxygen evolution electrocatalysts. *Energy Environ. Sci.* **16**, 5019–5028 (2023).
- Thangavel, P. et al. Immobilizing low-cost metal nitrides in electrochemically reconstructed platinum group metal (PGM)-free oxy-(hydroxides) surface for exceptional OER kinetics in anion exchange membrane water electrolysis. *Adv. Energy Mater.* **13**, 2203401 (2023).
- Ham, K., Hong, S., Kang, S., Cho, K. & Lee, J. Extensive active-site formation in trirutile CoSb₂O₆ by oxygen vacancy for oxygen evolution reaction in anion exchange membrane water splitting. *ACS Energy Lett.* **6**, 364–370 (2021).
- Han, X. et al. Metal–air batteries: from static to flow system. *Adv. Energy Mater.* **8**, 1801396 (2018).
- Lee, J. S. et al. Metal–air batteries with high energy density: Li–air versus Zn–air. *Adv. Energy Mater.* **1**, 34–50 (2011).
- Xie, Y. et al. High carbon utilization in CO₂ reduction to multi-carbon products in acidic media. *Nat. Catal.* **5**, 564–570 (2022).
- Gu, J. et al. Modulating electric field distribution by alkali cations for CO₂ electroreduction in strongly acidic medium. *Nat. Catal.* **5**, 268–276 (2022).
- García de Arquer, F. P. et al. CO₂ electrolysis to multicarbon products at activities greater than 1 A cm^{−2}. *Science* **367**, 661–666 (2020).
- Xue, Y. et al. Stabilizing ruthenium dioxide with cation-anchored sulfate for durable oxygen evolution in proton-exchange membrane water electrolyzers. *Nat. Commun.* **14**, 8093 (2023).
- Jeong, H.-Y. et al. High-performance water electrolyzer with minimum platinum group metal usage: Iron nitride–iridium oxide core–shell nanostructures for stable and efficient oxygen evolution reaction. *Appl. Catal. B Environ.* **330**, 122596 (2023).
- Fabbri, E. et al. Dynamic surface self-reconstruction is the key of highly active perovskite nano-electrocatalysts for water splitting. *Nat. Mater.* **16**, 925–931 (2017).

16. Han, S., Ryu, J. H., Lee, W. B., Ryu, J. & Yoon, J. translating the optimized durability of Co-based anode catalyst into sustainable anion exchange membrane water electrolysis. *Small* **20**, 2311052 (2024).
17. Liang, C. et al. Exceptional performance of hierarchical Ni-Fe oxyhydroxide@NiFe alloy nanowire array electrocatalysts for large current density water splitting. *Energy Environ. Sci.* **13**, 86–95 (2020).
18. Hu, C., Zhang, L. & Gong, J. Recent progress made in the mechanism comprehension and design of electrocatalysts for alkaline water splitting. *Energy Environ. Sci.* **12**, 2620–2645 (2019).
19. Han, S., Park, H. S. & Yoon, J. Superior performance of an anion exchange membrane water electrolyzer: sequential electro-deposited Co-based oxygen evolution catalyst. *Chem. Eng. J.* **477**, 146713 (2023).
20. Han, S., Park, J. & Yoon, J. Surface reconstruction of Co-based catalysts for enhanced oxygen evolution activity in anion exchange membrane water electrolysis. *Adv. Funct. Mater.* **34**, 2314573 (2024).
21. Chen, B., Biancolli, A. L. G., Radford, C. L. & Holdcroft, S. Stainless steel felt as a combined OER electrocatalyst/porous transport layer for investigating anion-exchange membranes in water electrolysis. *ACS Energy Lett.* **8**, 2661–2667 (2023).
22. Tricker, A. W. et al. Pathways toward efficient and durable anion exchange membrane water electrolyzers enabled by electro-active porous transport layers. *Adv. Energy Mater.* **14**, 2303629 (2023).
23. Costentin, C. & Nocera, D. G. Self-healing catalysis in water. *Proc. Natl. Acad. Sci. USA* **114**, 13380–13384 (2017).
24. Thorarindottir, A. E., Veroneau, S. S. & Nocera, D. G. Self-healing oxygen evolution catalysts. *Nat. Commun.* **13**, 1243 (2022).
25. Feng, C. et al. A self-healing catalyst for electrocatalytic and photoelectrochemical oxygen evolution in highly alkaline conditions. *Nat. Commun.* **12**, 5980 (2021).
26. Sun, Y. et al. Navigating surface reconstruction of spinel oxides for electrochemical water oxidation. *Nat. Commun.* **14**, 2467 (2023).
27. Chatti, M. et al. Intrinsically stable in situ generated electrocatalyst for long-term oxidation of acidic water at up to 80 °C. *Nat. Catal.* **2**, 457–465 (2019).
28. Surendranath, Y., Lutterman, D. A., Liu, Y. & Nocera, D. G. Nucleation, growth, and repair of a cobalt-based oxygen evolving catalyst. *J. Am. Chem. Soc.* **134**, 6326–6336 (2012).
29. Simondson, D. et al. Stable acidic water oxidation with a cobalt–iron–lead oxide catalyst operating via a cobalt-selective self-healing mechanism. *Angew. Chem. - Int. Ed.* **60**, 15821–15826 (2021).
30. Shinagawa, T., Ng, M. T. & Takanabe, K. Boosting the performance of the nickel anode in the oxygen evolution reaction by simple electrochemical activation. *Angew. Chem.* **129**, 5143–5147 (2017).
31. Krivina, R. A. et al. Anode catalysts in anion-exchange-membrane electrolysis without supporting electrolyte: conductivity, dynamics, and ionomer degradation. *Adv. Mater.* **34**, 2203033 (2022).
32. Mohammadi, M. R. et al. Exploring the limits of self-repair in cobalt oxide films for electrocatalytic water oxidation. *ACS Catal.* **10**, 7990–7999 (2020).
33. Anantharaj, S., Kundu, S. & Noda, S. “The Fe Effect”: a review unveiling the critical roles of Fe in enhancing OER activity of Ni and Co based catalysts. *Nano Energy* **80**, 105514 (2021).
34. Márquez, R. A. et al. Getting the basics right: preparing alkaline electrolytes for electrochemical applications. *ACS Energy Lett.* **8**, 1141–1146 (2023).
35. Ou, Y. et al. Cooperative Fe sites on transition metal (oxy)hydroxides drive high oxygen evolution activity in base. *Nat. Commun.* **14**, 7688 (2023).
36. Lopes, P. P. et al. Dynamically stable active sites from surface evolution of perovskite materials during the oxygen evolution reaction. *J. Am. Chem. Soc.* **143**, 2741–2750 (2021).
37. Shin, H., Yoo, J. M., Sung, Y. E. & Chung, D. Y. Dynamic electrochemical interfaces for energy conversion and storage. *JACS Au* **2**, 2222–2234 (2022).
38. Trotochaud, L., Young, S. L., Ranney, J. K. & Boettcher, S. W. Nickel-Iron oxyhydroxide oxygen-evolution electrocatalysts: the role of intentional and incidental iron incorporation. *J. Am. Chem. Soc.* **136**, 6744–6753 (2014).
39. Son, Y. J. et al. Effects of electrochemical conditioning on nickel-based oxygen evolution electrocatalysts. *ACS Catal.* **12**, 10384–10399 (2022).
40. Huang, W. et al. Oscillatory electrocatalytic oxidation of methanol on an Ni(OH)₂ film electrode. *J. Solid State Electrochem.* **9**, 284–289 (2005).
41. Yeo, B. S. & Bell, A. T. In situ Raman study of nickel oxide and gold-supported nickel oxide catalysts for the electrochemical evolution of oxygen. *J. Phys. Chem. C* **116**, 8394–8400 (2012).
42. Deng, J. et al. Morphology dynamics of single-layered Ni(OH)₂/NiOOH nanosheets and subsequent Fe incorporation studied by in situ electrochemical atomic force microscopy. *Nano Lett.* **17**, 6922–6926 (2017).
43. Bao, F. et al. Host, suppressor, and promoter—the roles of Ni and Fe on oxygen evolution reaction activity and stability of NiFe alloy thin films in alkaline media. *ACS Catal.* **11**, 10537–10552 (2021).
44. Gallenberger, J. et al. Stability and decomposition pathways of the NiOOH OER active phase of NiOx electrocatalysts at open circuit potential traced by ex situ and in situ spectroscopies. *Catal. Sci. Technol.* **13**, 4693–4700 (2023).
45. Payne, B. P., Biesinger, M. C. & McIntyre, N. S. The study of polycrystalline nickel metal oxidation by water vapour. *J. Electron Spectros. Relat. Phenom.* **175**, 55–65 (2009).
46. Moysiadiou, A., Lee, S., Hsu, C. S., Chen, H. M. & Hu, X. Mechanism of oxygen evolution catalyzed by cobalt oxyhydroxide: cobalt superoxide species as a key intermediate and dioxygen release as a rate-determining step. *J. Am. Chem. Soc.* **142**, 11901–11914 (2020).
47. Woo, J., Han, S. & Yoon, J. Mn-doped sequentially electrodeposited Co-based oxygen evolution catalyst for efficient anion exchange membrane water electrolysis. *ACS Appl. Mater. Interfaces* **16**, 23288–23295 (2024).
48. Han, S., Kim, S., Kim, T. H., Lee, J. Y. & Yoon, J. Optimizing the synergistic effect of Co and Fe for efficient and durable oxygen evolution under alkaline conditions. *ACS Appl. Mater. Interfaces* **16**, 35200–35207 (2024).
49. Lee, J. et al. High-efficiency anion-exchange membrane water electrolyzer enabled by ternary layered double hydroxide anode. *Small* **17**, 2100639 (2021).
50. Lee, S., Bai, L. & Hu, X. Deciphering iron-dependent activity in oxygen evolution catalyzed by nickel–iron layered double hydroxide. *Angew. Chem. Int. Ed.* **59**, 8072–8077 (2020).
51. Steimecke, M., Seiffarth, G. & Bron, M. In situ characterization of Ni and Ni/Fe thin film electrodes for oxygen evolution in alkaline media by a Raman-coupled scanning electrochemical microscope setup. *Anal. Chem.* **89**, 10679–10686 (2017).
52. Klaus, S., Cai, Y., Louie, M. W., Trotochaud, L. & Bell, A. T. Effects of Fe electrolyte impurities on Ni(OH)₂/NiOOH structure and oxygen evolution activity. *J. Phys. Chem. C* **119**, 7243–7254 (2015).
53. Ferriday, T. B. et al. Tuning stainless steel oxide layers through potential cycling—AEM water electrolysis free of critical raw materials. *ACS Appl. Mater. Interfaces* **16**, 29963–29978 (2024).
54. Zuo, Y. et al. Stainless steel activation for efficient alkaline oxygen evolution in advanced electrolyzers. *Adv. Mater.* **36**, 2312071 (2024).
55. Han, S., Ryu, J. & Yoon, J. Intermittent polarity inversion of stainless-steel paired electrodes for efficient and durable water electrolysis. *Chem. Eng. J.* **501**, 157603 (2024).
56. Kim, S. et al. High-performance and durable anion-exchange membrane water electrolyzers with high-molecular-weight

- polycarbazole-based anion-conducting polymer. *Energy Environ. Sci.* **17**, 5399–5409 (2024).
57. Lindquist, G. A., Xu, Q., Oener, S. Z. & Boettcher, S. W. Membrane electrolyzers for impure-water splitting. *Joule* **4**, 2549–2561 (2020).

Acknowledgements

This work was supported by the National Research Foundation of Korea (NRF) grant funded by the Korea government (MSIT) (RS-2024-00449579) awarded to J.Y. and the Institute for Basic Science (IBS-R006-D1) for J.R. Additionally, J.R. acknowledges the NRF grant funded by the Korean Government (MSIT) (RS-2024-00348577, RS-2024-00415940, and RS-2024-00421181) and the Creative-Pioneering Researchers Program (0458-20240094) through Seoul National University (SNU). J.Y.L. acknowledges the NFR grant funded by the Nano & Material Technology Development Program by the Ministry of Science and ICT (RS-2024-00409675). We appreciate Prof. Jungwon Park at SNU for supporting Raman spectroscopy analyses. We appreciate the staff and crew of the National Center for Inter-university Research Facilities (NCIRF) at SNU for their advice and assistance in SEM and XPS analyses.

Author contributions

S.H., J.R., and J.Y. conceived the research and wrote the paper. S.H. performed the most experiments and material analyses. S.K. conducted the 3-cell stack experiment. H.C. and J.Y.L. synthesized and characterized the HQPC-TMA membrane. J.Y.L., J.R., and J.Y. supervised the project. All authors participated in and contributed to the final version.

Competing interests

The authors declare no competing interests.

Additional information

Supplementary information The online version contains supplementary material available at <https://doi.org/10.1038/s41467-025-60201-w>.

Correspondence and requests for materials should be addressed to Jang Yong Lee, Jaeyune Ryu or Jeyong Yoon.

Peer review information *Nature Communications* thanks Yu Seung Kim and the other anonymous reviewers for their contribution to the peer review of this work. A peer review file is available.

Reprints and permissions information is available at <http://www.nature.com/reprints>

Publisher's note Springer Nature remains neutral with regard to jurisdictional claims in published maps and institutional affiliations.

Open Access This article is licensed under a Creative Commons Attribution-NonCommercial-NoDerivatives 4.0 International License, which permits any non-commercial use, sharing, distribution and reproduction in any medium or format, as long as you give appropriate credit to the original author(s) and the source, provide a link to the Creative Commons licence, and indicate if you modified the licensed material. You do not have permission under this licence to share adapted material derived from this article or parts of it. The images or other third party material in this article are included in the article's Creative Commons licence, unless indicated otherwise in a credit line to the material. If material is not included in the article's Creative Commons licence and your intended use is not permitted by statutory regulation or exceeds the permitted use, you will need to obtain permission directly from the copyright holder. To view a copy of this licence, visit <http://creativecommons.org/licenses/by-nc-nd/4.0/>.

© The Author(s) 2025